Value-added by high-resolution regional simulations of climate-relevant aerosol properties

P. Crippa[1], R. C. Sullivan[2], A. Thota[3], S. C. Pryor[2,3]

[1]COMET, School of Civil Engineering and Geosciences, Cassie Building, Newcastle University, Newcastle upon Tyne, NE1 7RU, UK

[2]Department of Earth and Atmospheric Sciences, Bradfield Hall, 306 Tower Road, Cornell University, Ithaca, NY 14853, USA

[3]Pervasive Technology Institute, Indiana University, Bloomington, IN 47405, USA

Correspondence to: P. Crippa (paola.crippa@ncl.ac.uk), School of Civil Engineering and Geosciences, Cassie Building, Room G15, Telephone: +44 (0)191 208 5041, Newcastle University, Newcastle upon Tyne, NE1 7RU, UK

16   **Abstract**

17   Despite recent advances in global Earth System Models (ESMs), the current global mean
18   aerosol direct and indirect radiative effects remain uncertain, as does their future role in climate
19   forcing and regional manifestations. Reasons for this uncertainty include the high spatio-
20   temporal variability of aerosol populations. Thus, limited area (regional) models applied at
21   higher resolution over specific regions of interest are generally expected to 'add value', i.e.
22   improve the fidelity of the physical-dynamical-chemical processes that induce extreme events
23   and dictate climate forcing, via more realistic representation of spatio-temporal variability.
24   However, added value is not inevitable, and there remains a need to optimize use of numerical
25   resources, and to quantify the impact on simulation fidelity that derives from increased
26   resolution. Here we quantify the value added by enhanced spatial resolution in simulations of
27   the drivers of aerosol direct radiative forcing by applying the Weather Research and
28   Forecasting model with coupled Chemistry (WRF-Chem) over eastern North America at
29   different resolutions. Using Brier Skill Scores and other statistical metrics it is shown that
30   enhanced resolution (from 60 to 12 km) improves model performance for all of the
31   meteorological parameters and gas phase concentrations considered, in addition to both mean
32   and extreme Aerosol Optical Depth (AOD) in three wavelengths in the visible relative to
33   satellite observations, principally via increase of potential skill. Some of the enhanced model
34   performance for AOD appears to be attributable to improved simulation of specific humidity
35   and the resulting impact on aerosol hygroscopic growth/hysteresis.

36

37   **Keywords:** added value, high-resolution WRF-Chem simulations, aerosol optical properties,
38   extreme AOD

1 Motivation and Objectives

Aerosols alter Earth's radiation balance primarily by scattering or absorbing incoming solar radiation (direct effect, dominated by accumulation mode (diameters ~ wavelength (λ), where total extinction is often quantified using AOD), or regulating cloud formation/properties by acting as cloud condensation nuclei (CCN) (indirect effect, dominated by diameters $\geq$ 100 nm, magnitude = f(composition)). Most aerosols (excluding black carbon) have a larger scattering cross-section than absorption cross-section, and act as CCN thus enhancing cloud albedo and lifetimes. Hence increased aerosol concentrations are generally (but not uniformly) associated with surface cooling (offsetting a fraction of greenhouse gas warming) (Boucher, 2013;Myhre et al., 2013b) to a degree that is principally dictated by the aerosol concentration, size and composition, in addition to the underlying surface and height of the aerosol layer (McComiskey et al., 2008). Despite major advances in measurement and modeling, both the current global mean aerosol direct effect (possible range: -0.77 to +0.23 W m^{-2}) and the indirect effect (possible range: -1.33 to -0.06 W m^{-2}) remain uncertain (Stocker, 2013), as does their future role in climate forcing (Rockel et al., 2008) and regional manifestations (Myhre et al., 2013a). Specific to our current study region (eastern N. America), one analysis using the NASA GISS global model found that the "regional radiative forcing from US anthropogenic aerosols elicits a strong regional climate response, cooling the central and eastern US by 0.5–1.0 °C on average during 1970–1990, with the strongest effects on maximum daytime temperatures in summer and autumn. Aerosol cooling reflects comparable contributions from direct and indirect radiative effects" (Leibensperger et al., 2012). A recent comparison of multiple global models conducted under the AEROCOM-project indicated this is also a region that exhibits very large model-to-model variability in simulated AOD (<AOD> ~ 0.5, σ(AOD) ~ 1) (Myhre et al., 2013a).

Major reasons why aerosol radiative forcing on both the global and regional scales remains uncertain include short atmospheric residence times and high spatio-temporal variability of aerosol populations, and the complexity of the processes that dictate aerosol concentrations, composition and size distributions (Seinfeld and Pandis, 2016). Although aerosol processes and properties are increasingly being treated in the global Earth System Models (ESMs) (Long et al., 2015;Tilmes et al., 2015) being applied in Coupled Model Intercomparison Project Phase 6 (CMIP-6) (Meehl et al., 2014), the scales on which such models are applied remain much coarser than those on which aerosol population properties are known to vary (Anderson et al., 2003). Therefore, limited area atmospheric models (regional models) applied at higher

72 resolution over specific regions of interest are expected to 'add value' (i.e. improve the fidelity)

73 of the physical-dynamical-chemical processes that induce extreme events and dictate climate

74 forcing. There is empirical evidence to suggest strong resolution dependence in simulated

75 aerosol particle properties. For example, WRF-Chem simulations with spatial resolution

76 enhanced from 75 km to 3 km exhibited higher correlations and lower bias relative to

77 observations of aerosol optical properties over Mexico likely due to more accurate description

78 of emissions, meteorology and of the physicochemical processes that convert trace gases to

79 particles (Gustafson et al., 2011;Qian et al., 2010). This improvement in the simulation of

80 aerosol optical properties implies, a reduction of the uncertainty in associated aerosol radiative

81 forcing (Gustafson et al., 2011). Further, WRF-Chem run over the United Kingdom and

82 Northern France at multiple resolutions in the range of 40-160 km, underestimated AOD by

83 10-16% and overestimated CCN by 18-36% relative to a high resolution run at 10 km, partly

84 as a result of scale dependence of the gas-phase chemistry and differences in the aerosol uptake

85 of water (Weigum et al., 2016).

86 However, debate remains regarding how to objectively evaluate model performance, quantify

87 the value added by enhanced resolution (Di Luca et al., 2015;Rockel et al., 2008) and on

88 possible limits to the improvement of climate representation in light of errors in the driving

89 "imperfect lateral boundary conditions" (Diaconescu and Laprise, 2013). Nevertheless,

90 although "it is unrealistic to expect a vast amount of added values since models already

91 performs rather decently" (Di Luca et al., 2015) and global ESMs are now run at much higher

92 resolution than in the past, it is generally assumed that high resolution regional models will add

93 value via more realistic representation of spatio-temporal variability than global coarser-

94 resolution simulations. Further, "the main added value of a regional climate model is provided

95 by its small scales and its skill to simulate extreme events, particularly for precipitation"

96 (Diaconescu and Laprise, 2013).

97 Here we quantify the value added by enhanced resolution in the description of the drivers of

98 aerosol direct radiative forcing using year-long simulations from WRF-Chem over eastern

99 North America. The primary performance evaluation focuses on AOD at different wavelengths

100 ($\lambda = 470$, 550 and 660 nm, where the AOD at different λ is used as a proxy of the aerosol size

101 distribution (Tomasi et al., 1983), see details in Sect. 2.1) and is measured relative to

102 observations from satellite-borne instrumentation. Thus the term "value added" is used here to

103 refer to an improvement of model performance in simulation of wavelength specific AOD as

104 measured by the MODerate resolution Imaging Spectroradiometer (MODIS) instrument

105 aboard the polar-orbiting Terra satellite. We begin by quantifying the performance of WRF-
106 Chem when applied over eastern North America at a resolution of 60 km (WRF60) (~ finest
107 resolution likely to be employed in CMIP-6 global simulations) and then compare the results
108 to those from simulations conducted at 12 km (WRF12) (simulation details are given in Table
109 1). Quantification of model skill is undertaken by mapping the WRF12 output to the WRF60
110 grid (WRF12-remap) and computing Brier Skill Scores (BSS) using MODIS as the target,
111 WRF60 as the reference forecast and WRF12-remap as the forecast to be evaluated. We also
112 evaluate the impact of simulation resolution on extreme AOD values that are associated with
113 enhanced impacts on climate and human health. This analysis uses both *Accuracy* and *Hit Rate*
114 as the performance metrics and focuses on the co-occurrence of extreme values in space from
115 the model output and MODIS.

116 Our final analysis focuses on evaluation of the value-added by enhanced resolution in terms of
117 key meteorological and gas-phase drivers of aerosol concentrations and composition and is
118 conducted relative to the MERRA-2 reanalysis product for the physical variables and columnar
119 gas concentrations from satellite observations (see details of the precise data sets used given
120 below). The meteorological parameters considered are air temperature at 2 m (T_{2m}), total
121 monthly precipitation (*PPT*), planetary boundary-layer height (*PBLH*) and specific humidity
122 in the boundary layer (Q_{PBL}). The gas phase concentrations considered are: sulfur dioxide
123 (SO_2), ammonia (NH_3), nitrogen dioxide (NO_2) and formaldehyde (HCHO).

124 **2 Materials and Methods**

125 **2.1 Spectral dependence of AOD**

126 Three properties dictate the actual aerosol direct radiative forcing: AOD, single scattering
127 albedo and asymmetry factor, all of which are a function of the wavelength (λ) of incident
128 radiation. The first property is related to the total columnar mass loading, typically dominates
129 the variability of direct aerosol effect (Chin et al., 2009) and is the focus of the current research.
130 The relationship between the aerosol size distribution and spectral dependence of AOD is
131 described by a power law function:

132
$$\beta(\lambda_1) = \beta(\lambda_2) \times \frac{\lambda_1}{\lambda_2}^{-\alpha} \quad \text{(1)}$$

133 where β is the particle extinction coefficient at a specific wavelength λ and α is the Ångström

134   exponent (Ångström, 1964) which describes the wavelength dependence of AOD (and is

135   inversely proportional to the average aerosol diameter):

136    $$\alpha = \frac{\ln \dfrac{AOD(\lambda_1)}{AOD(\lambda_2)}}{\dfrac{\lambda_2}{\lambda_1}} \quad (2)$$

137   The aerosol volume distribution (and thus also its size distribution) usually conforms to a multi-

138   lognormal function with n modes:

139    $$\frac{dV(r)}{d\ln r} = \sum_{i=1}^{n} \frac{C_i}{\sqrt{2\pi}\sigma_i} \exp\left[\frac{-(\ln r - \ln R_i)^2}{2\sigma_i^2}\right] \quad (3)$$

140   where C_i is the particle volume concentration in the mode i, R_i is the geometric mean radius

141   and σ_i is the geometric standard deviation, thus we have:

142

143    $$AOD(\lambda) = \int \frac{3\beta(m,r,\lambda)}{4r} \frac{dV(r)}{d\ln r} d\ln r dZ \quad (4)$$

144   As indicated in (Schuster, 2006), "the spectral variability of extinction diminishes for particles

145   larger than the incident wavelength", thus fine mode particles contribute more to AOD in the

146   visible ($\lambda \sim 0.5$ µm) than at longer wavelengths, whereas coarse mode particles provide a similar

147   AOD both at short and long wavelengths. This is reflected in the Ångström parameter which

148   can be thus used as a proxy for the fine mode fraction or fine mode radius (Schuster, 2006).

149   **2.2 WRF-Chem simulations**

150   WRF-Chem (version 3.6.1) simulations were performed for the calendar year 2008 over eastern

151   North America, in a domain centered over southern Indiana (86°W, 39°N) at two resolutions,

152   one close to the finest resolution designed for CMIP-6 global model runs (i.e. 60 km, WRF60)

153   and the other one at much higher resolution (12 km, WRF12). Simulation settings are identical

154   for the two runs except for the time-step used for the physics (Table 1). Physical and chemical

155   parameterizations were chosen to match previous work using WRF-Chem at 12 km on the same

156   region which showed good performance relative to observations and the year 2008 was selected

157   because representative of average climate and aerosol conditions during 2000 - 2014 (Crippa

158   et al., 2016). More specifically the simulations adopted the RADM2 chemical mechanism

159   (Stockwell et al., 1990) and a modal representation of the aerosol size distribution

160   (MADE/SORGAM, (Ackermann et al., 1998;Schell et al., 2001)) with three lognormal modes

161   and fixed geometric standard deviations (i.e. 1.7, 2 and 2.5 for Aitken, accumulation and coarse

162   mode, respectively (Ackermann et al., 1998;Grell et al., 2005)). Aerosol direct feedback was

163   turned on and coupled to the Goddard shortwave scheme (Fast et al., 2006). A telescoping

164   vertical grid with 32 model layers from the surface to 50 hPa and 10 layers up to 800 hPa was

165   selected. Meteorological initial and boundary conditions from the North American Mesoscale

166   Model at 12 km resolution are applied every 6 hours, while initial and chemical boundary

167   conditions are taken from MOZART-4 (Model for Ozone and Related chemical Tracers,

168   version 4) with meteorology from NCEP/NCAR-reanalysis (Emmons et al., 2010).

169   Anthropogenic emissions are specified for both WRF60 and WRF12 from the US National

170   Emission Inventory 2005 (NEI-05) (US-EPA, 2009) which provides hourly point and area

171   emissions at 4 km on 19 vertical levels. The simulation settings and specifically the use of a

172   modal representation of the aerosol size distribution were selected to retain computational

173   tractability. Accordingly, the 60 km simulations for the year 2008 completed in 6.4 hours

174   whereas the 12 km simulations completed in 9.5 days (230 hours) on the Cray XE6/XK7

175   supercomputer (Big Red II) owned by Indiana University, using 256 processors distributed on

176   8 nodes.

177   Value added is quantified by degrading (averaging) hourly output from the 12 km resolution

178   simulation to 60 km (hereafter WRF12-remap) as follows: the 12 km domain is resized

179   excluding 2 grid cells at the border to exactly match the 60 km resolution domain. Each coarse

180   grid cell thus includes 5×5 12 km resolution cells and its value is the mean of all valid 12 km

181   grid cells inside it if at least half of those cells contain valid AOD (i.e. no cloud cover),

182   otherwise the whole coarse cell is treated as missing. In all comparisons only cells with

183   simultaneous (i.e. model and MODIS) clear sky conditions are considered. A daily value from

184   WRF-Chem is computed as an instantaneous value for the hour nearest to the satellite overpass

185   time. When the comparison is done on a monthly basis, a monthly mean value is computed

186   from the daily values obtained under clear sky conditions, only if there are at least five valid

187   observations in the month.

188   **2.3 Observations**

189   Model aerosol optical properties are evaluated relative to the MODIS Collection 6 dark-target

190   land aerosol product from aboard the Terra satellite (~1030 overpass local solar time (LST))

191   (Levy et al., 2013). To provide a consistent assessment of model skill, the evaluation of AOD

is conducted only on land areas since the MODIS dark-target ocean aerosol product is based on a retrieval algorithm different from the one over land (Levy et al., 2013). Trace gas concentrations are evaluated relative to measurements from the Ozone Monitoring Instrument (OMI; version 3) (Chance, 2002) and the Infrared Atmospheric Sounding Interferometer (IASI; NN version 1) (Whitburn, 2016) aboard the Aura (~1345 LST) and MetOp satellites (~0930 LST), respectively. MODIS retrieves AOD at multiple λ including 470, 550, and 660 nm, and the MODIS algorithm removes cloud-contaminated pixels prior to spatial averaging over 10×10 km (at nadir). OMI and IASI have nadir resolutions of 13×24 km and 12 km (circular footprint), respectively, and have been filtered to remove retrievals with cloud fractions > 0.3 (Fioletov et al., 2011;McLinden et al., 2014;Vinken et al., 2014) and OMI pixels affected by the row anomalies. MODIS, OMI, and IASI provide near daily global coverage, although the row anomalies render portions of the OMI viewing swath unusable. Uncertainty in AOD from MODIS is spatially and temporally variable. It has been estimated as $\pm (0.05 + 15\%)$ for AOD over land (Levy et al., 2013), and prior research has reported 71% of MODIS Collection 5 retrievals fall within $0.05 \pm 20\%$ for AOD relative to AERONET in the study domain (Hyer et al., 2011). The accuracy of OMI ("root sum of the square of all errors, including forward model, inverse model, and instrument errors" (Brinksma, 2003)) is 1.1 DU or 50% for SO_2, 2×10^{14} cm^{-2}/30% for background/polluted NO_2 conditions, and 35% for HCHO. This uncertainty is typically reduced by spatial and temporal averaging, as employed herein (Fioletov et al., 2011;Krotkov et al., 2008). IASI NH_3 retrievals do not use an a priori assumption of emissions, vertical distribution, or lifetime of NH_3 (i.e. no averaging kernel); therefore, NH_3 accuracy is variable, and thus only retrievals with uncertainty lower than the retrieved concentrations are used (Whitburn, 2016).

For the model evaluation, satellite observations for each day are regridded to the WRF-Chem discretization. This is done by averaging all valid retrievals within: 0.1° and 0.35° of the WRF-Chem grid-cell center for the 12×12 km and 60×60 km resolutions, respectively for MODIS; 0.125° × 0.18° (along-track/latitudinal × cross-track/longitudinal) and 0.365° × 0.42° for OMI; 0.12° and 0.36° for IASI,. To avoid issues from under-sampling, we require at least 10 valid MODIS granules for the 60×60 km daily average to be computed and at least 5 daily averages to compute a monthly average for each grid cell. Model evaluation of gaseous species is performed on a seasonal basis using standard scores (z-scores), which are computed as the difference between the seasonal mean within a grid cell and the seasonal spatial mean, divided by the seasonal spatial standard deviation. The use of standard scores allows comparison of the

spatial patterns of satellite observations and model output in terms of standard deviation units from the mean.

The simulated meteorological properties are evaluated using Modern-Era Retrospective analysis for Research and Applications (MERRA-2) reanalysis data as the target. MERRA-2 is a homogenized and continuous in time description of atmospheric properties on a 3-dimensional global grid (horizontal resolution of 0.5°×0.625°, L72), developed by NASA and was released in Fall 2015 (Molod et al., 2015). MERRA-2 provides hourly values of T_{2m} and *PBLH*, and vertical profile of 3-dimensional variables every 3 hours on a large number of pressure levels. Here we compute the total specific humidity (Q_{PBL}) of the lowest 8 pressure levels (i.e. in the boundary-layer approximated as the layer from 1000 to 825 hPa) in MERRA-2, assuming an average air density in the PBL of 1.1 kg m^{-3}. For the evaluation of simulated precipitation, we use accumulated monthly total values.

2.4 Quantification of model performance and added-value

Taylor diagrams summarize three aspects of model performance relative to a reference: the spatial correlation coefficient (i.e. Pearson correlation of the fields, r), the ratio of spatial standard deviations of the two spatial fields ($\sigma_{wrf}/\sigma_{sat}$) and the root mean squared difference (Taylor, 2001). Here Taylor diagrams are presented for monthly mean AOD from WRF60, WRF12 and WRF12-remap relative to MODIS at different wavelengths (Fig. 1 d-f). Because AOD is not normally distributed, Spearman's rank correlation coefficients (ρ) of the mean monthly AOD spatial fields are also computed to reduce the impact of a few outliers and the small sample size during cold months (Table 2). To assess the significance of ρ while accounting for multiple testing, we apply a Bonferroni correction (Simes, 1986) in which for *m* hypothesis tests, the null hypothesis is rejected if $p \leq \dfrac{\alpha}{m}$, where *p* is the p-value and α is the confidence level (0.05 is used here).

We further quantify the value added (or lack of thereof) of the high-resolution simulations using the following metrics:

(i) Brier Skill Score

The primary metric used to quantify the added value of WRF12-remap versus WRF60 is the Brier Skill Score (BSS) (Murphy and Epstein, 1989):

$$BSS = \frac{r_{F'P'}^2 - \left(r_{F'P'} - \frac{\sigma_{F'}}{\sigma_{P'}}\right)^2 - \left(\frac{\langle P'\rangle - \langle F'\rangle}{\sigma_{P'}}\right)^2 + \left(\frac{\langle P'\rangle}{\sigma_{P'}}\right)^2}{1 + \left(\frac{\langle P'\rangle}{\sigma_{P'}}\right)^2} \quad \textbf{(5)}$$

where F is the "forecast" (i.e. the 12 km simulations mapped to 60 km, WRF12-remap); P is the "target" (i.e. MODIS at 60 km) and output from WRF60 are used as the reference forecast; F' the difference between 12 km estimates regridded to 60 km and MODIS; P' the difference between the 60 km simulation and MODIS.

BSS measure how much a test simulation (i.e. WRF12-remap) more closely (or poorly) reproduces observations (from MODIS, MERRA-2 or other satellite products) relative to a control (WRF60) run. A BSS>0 indicates WRF12, even when regridded to 60 km, does add value. The first term in (5) ranges from 0 to 1, is described as the potential skill, and is the square of the spatial correlation coefficient between forecast and reference anomalies to MODIS. It is the skill score achievable if both the conditional bias (second term) and overall bias (third term) were zero, and for most of the variables considered herein (particularly AOD) it contributes to a positive BSS in most calendar months (and seasons). The second term (the conditional bias, > 0), is the square of the difference between the anomaly correlation coefficient and the ratio of standard deviation of the anomalies and is small if for all points F' is linear to P'. The third term is referred to as the forecast anomaly bias, and is the ratio of the difference between the mean anomalies of WRF12-remap and the observations relative to WRF60 and the standard deviation of WRF60 anomaly relative to observed values. The fourth term is the degree of agreement and appears in both the numerator and denominator. It is computed as the square of the ratio of the mean anomaly between WRF60 and observations and the standard deviation of the anomalies.

(ii) Pooled paired t-test

To identify which areas in space contribute most to the added value, we compare daily mean AOD fields from WRF-Chem at different resolutions and MODIS. We perform a pooled paired t-test to evaluate the null hypothesis that those differences come from normal distributions with equal means and equal but unknown variances (the test statistic has a Student's t distribution with df $=$ n $+$ m $-$ 2, and the sample standard deviation is the pooled standard deviation, where n and m are the two sample sizes). The test is conducted by climatological season (e.g. winter $=$ DJF) since there are fewer than 20 valid AOD observations in most 60 km grid cells for each

283 calendar month (Fig. 2). Given the large number of hypothesis tests performed (i.e. one for
284 each 60 km grid cell), we adjust the p-values using the False Discovery Rate (FDR) approach
285 (Benjamini and Hochberg, 1995). In this approach, p-values from the t-tests are ranked from
286 low to high ($p_1, p_2, \ldots, p_m$), then the test with the highest rank, j, satisfying:

287 $$p_j \leq \frac{j}{m} \alpha \quad \textbf{(6)}$$

288 is identified. Here all p-values satisfying Eq. 6 with $\alpha=0.1$ are considered significant.

289 **(iii) Accuracy and Hit Rate in identification of extremes**

290 For each month we identify grid cells in which the wavelength specific AOD exceeds the 75th
291 percentile value computed from all grid cells and define that as an extreme. Thus grid cells
292 with extreme AOD are independently determined for MODIS and WRF-Chem at different
293 resolutions. The spatial coherence in identification of extremes in the fields is quantified using
294 two metrics: the *Accuracy* and the *Hit Rate* (*HR*). The *Accuracy* indicates the overall spatial
295 coherence and is computed as the number of grid cells co-identified as extreme and non-
296 extreme between WRF-Chem and MODIS relative to the total number of cells with valid data.
297 The *HR* weights only correct identification of extremes in MODIS by WRF-Chem.

298 **3 Results**

299 **3.1 Quantifying the value added of increased spatial resolution**

300 When WRF-Chem is applied at 60 km resolution the degree of association of the resulting
301 spatial fields of mean monthly AOD at the three wavelengths with MODIS varies seasonally.
302 Smallest RMSD and highest Spearman spatial correlations (ρ) with MODIS observations
303 generally occur during months with highest mean AOD (i.e. during summer, Fig. 1 d-f and Fig.
304 3), and reach a maximum in August ($\rho = 0.60$, Table 2). However, while the patterns of relative
305 AOD variability are well captured, the absolute magnitudes and spatial gradients of AOD
306 during the summer are underestimated by WRF60 (Fig. 1 d-f and Fig. 3, Table S1). High spatial
307 correlations ($\rho > 0.40$) are also observed in March, April and November (Table 2), when the
308 ratio of spatial standard deviations is closer to 1 (Fig. 1 d-f, Table S1). Only a weak wavelength
309 dependence is observed in the performance metrics as described on Taylor diagrams. The
310 spatial variability is generally more negatively biased for AOD at 660 nm (Table S1), indicating
311 that WRF60 simulations tend to produce larger diameter aerosols homogeneously distributed
312 over the domain, whereas MODIS observations indicate more spatial variability.

The performance of WRF60 simulations relative to MODIS contrasts with analyses of WRF12 and WRF12-remap. WRF12 and WRF12-remap indicate highest spatial correlations with MODIS observations throughout the summer months (ρ = 0.5-0.7, Table 2), although the bias towards simulation of more coarse aerosols than are observed is consistent across the two simulations and with prior research (see details provided in (Crippa et al., 2016)). However, simulations at 12 km (WRF12) show positive ρ with MODIS for all λ in all calendar months, while mean monthly spatial fields of AOD from WRF60 show low and/or negative correlations with MODIS during May, June, September, October and December, indicating substantial differences in the degree of correspondence with MODIS AOD in the two simulations, and higher fidelity of the enhanced resolution runs (Tables 2 and S1).

Monthly mean spatial fields of AOD(λ) as simulated by WRF12 or WRF12-remap exhibit positive Spearman correlation coefficients (ρ) with MODIS observations for all calendar months and range from ~ 0.25 for WRF12-remap (0.20 for WRF12) during winter to ~ 0.70 and 0.64, respectively during summer (Table 2). Spearman's ρ are uniformly higher in WRF12-remap than WRF12 indicating a mismatch in space in the high-resolution simulation (i.e. that grid cells with high AOD are slightly displaced in the 12 km simulations possibly due to the presence of sub-grid scale aerosol plumes (Rissman et al., 2013)). Mean monthly fields of AOD (all λ) from both WRF12 and WRF12-remap exhibit lower ρ with MODIS in February-April and November than the 60 km runs (Table 2). These discrepancies appear to be driven by conditions in the south of the domain. For example, differences between WRF60/WRF12-remap vs. MODIS during all seasons are significant according to the paired t-test over Florida and along most of the southern coastlines (Fig. 2). This region of significant differences extends up to ~ 40°N during summer and fall, reflecting the stronger north-south gradient in AOD from MODIS and WRF12-remap that is not captured by WRF60 (see example for λ = 550 nm, Fig. 3). These enhancements in the latitudinal gradients from WRF12-remap are also manifest in the physical variables (particularly specific humidity as discussed further below).

The differences in the absolute values of mean monthly AOD deriving from differences in the resolution at which WRF-Chem was applied are of sufficient magnitude (a difference of up to 0.2 in regions with a mean AOD value of 0.4), particularly in the summer months (Fig. 4), to raise concerns. However, detailed investigation of the simulations settings and repetition of the 60 km simulation resulted in virtually identical results indicating no fault can be found in the analysis. Further, we note that the eastern-half of North America was also identified as a region

345   of high discrepancy in global ESM (Myhre et al., 2013a).

346   To further investigate differences in the simulation output due to spatial discretization we

347   computed Brier Skill Scores (BSS). In this analysis AOD for each λ from WRF12-remap are

348   used as the 'forecast', output from WRF60 are used as the reference forecast and MODIS

349   observations at 60 km are used as the target. BSS exceed 0 during all months except for

350   September and October, and largest BSS (> 0.5) for AOD (all λ) is found during most months

351   between December and July (Fig. 5). This indicates that running WRF-Chem at 12 km

352   resolution adds value relative to WRF60, even when the WRF12 output is remapped to 60 km.

353   BSS do not strongly depend on λ, indicating the added value from enhanced resolution

354   similarly affects particles of different sizes. Inspecting the terms defining the BSS provides

355   information about the origin of the added value (Fig. 5). The positive BSS derives principally

356   from the potential skill (first term in Eq. 5), which demonstrates a reduction in bias and/or more

357   accurate representation of the spatial gradients in WRF12-remap. This term exhibits weak

358   seasonality with values below 0.5 only during August and fall months. The second and third

359   terms are close to zero during most months, although bigger biases are found during August-

360   October. The substantial conditional bias during late summer and early fall is the result of the

361   large ratio of standard deviations (> 1, i.e. the spatial variability of the anomaly relative to

362   MODIS is larger for WRF12-remap than WRF60, Table S1). It thus contributes to the negative

363   BSS found in September and October, which are also identified as outlier months in WRF12-

364   remap from the Taylor diagram analysis (Fig. 1). Output for these months show modest spatial

365   correlations with MODIS and higher ratio of standard deviations than in WRF60-MODIS

366   comparisons (Fig. 1, Table S1). Previous work showed that the lower model skill (in WRF12)

367   during September and October may be partially attributable to a dry bias in precipitation from

368   WRF-Chem relative to observations. As a result, simulated AOD and near-surface aerosol

369   nitrate and sulfate concentrations are positively biased over large parts of the domain (Crippa

370   et al., 2016).

371   Model resolution also affects the *Accuracy* and *Hit Rate* (*HR*) for identification of areas of

372   extreme AOD (AOD>75th percentile). Highest coherence in the identification of extreme AOD

373   in space identified in WRF12-remap (and WRF12) relative to MODIS is found during May-

374   August (*HR* = 53-77%) vs. WRF60 (*HR* = 17-54%, Table 3). Conversely highest *HR* are found

375   for WRF60 and MODIS during winter and early spring, and indeed exceed those for WRF12

376   and WRF12-remap (Table 3, e.g. Feb: *HR* = 0.78 for WRF60, and 0.67 and 0.68 for WRF12

377   and WRF12-remap, respectively). These differences are consistent with the observation that

378   WRF12-remap overestimates the scales of AOD coherence and AOD magnitude during the
379   cold season along coastlines and over much of the domain in April (Fig. 3).

380   The synthesis of these analyses is thus that the higher resolution simulation increases the
381   overall spatial correlation, decreases overall bias in AOD close to the peak of the solar spectrum
382   relative to MODIS observations and therefore the higher-resolution simulations better
383   represent aerosol direct climate forcing. However, WRF12-remap exhibits little improvement
384   over WRF60 in terms of reproducing the spatial variability of AOD in the visible wavelengths
385   and further that WRF12-remap tends to be more strongly positively biased in terms of mean
386   monthly AOD outside of the summer months (Fig. 2 and Fig. 3). Also the improvement in
387   detection of areas of extreme AOD in the higher resolution simulations (WRF12-remap) is
388   manifest only during the warm season.

389   **3.2 Investigating the origin of the added value and sources of error in simulated AOD**

390   As documented above, WRF-Chem applied at either 60 or 12 km resolution over eastern North
391   America exhibits some skill in reproducing observed spatial fields of AOD and the occurrence
392   of extreme AOD values. However, marked discrepancies both in space and time are found, and
393   at least some of them show a significant dependence on model resolution. Thus, we
394   investigated a range of physical conditions and gas phase concentrations known to be strongly
395   determinant of aerosol dynamics in terms of the BSS as a function of model resolution and also
396   in terms of the mean monthly spatial patterns.

397   WRF12 even when remapped to 60 km provides more accurate description of key
398   meteorological variables such as specific humidity (Q) within the boundary layer, *PBLH*,
399   surface temperature and precipitation (Fig. 6, S1, S2 and S3) when compared to MERRA-2, as
400   indicated by the positive BSS during almost all months (Fig. 7a). Good qualitative agreement
401   is observed for the spatial patterns and absolute magnitude of T_{2m} in both WRF60 and WRF12-
402   remap relative to MERRA-2 for all seasons (Fig. S1) leading to only modest magnitude of BSS
403   (i.e. value added by the higher resolution simulations (Fig. 7a)). The aerosol size distribution
404   and therefore wavelength specific AOD exhibits a strong sensitivity to Q (Santarpia et al.,
405   2005) due to the presence of hygroscopic components in atmospheric aerosols and thus the role
406   of water uptake in determining aerosol diameter, refractivity and extinction coefficient (Zieger
407   et al., 2013). For example, the hygroscopic growth factor, which indicates the change of aerosol
408   diameter due to water uptake, is ~ 1.4 for pure ammonium sulfate with dry diameter of 532 nm
409   at relative humidity of 80%, thus biases in representation atmospheric humidity may lead to

big errors in simulated aerosol size and AOD (Flores et al., 2012). Our previous analyses of the 12 km resolution simulations indicated overestimation of sulfate aerosols (a highly hygroscopic aerosol component, and one which in many chemical forms exhibits strong hysteresis (Martin et al., 2004)) relative to observed near-surface PM$_{2.5}$ concentrations during all seasons except for winter (Crippa et al., 2016), leading to the hypothesis that simulated AOD and discrepancies therein may exhibit a strong dependence on Q. Consistent with that postulate, Q_{PBL} from WRF12-remap exhibits a moist bias in cloud-free grid cells mostly during warm months, whereas WRF60 is characterized by a dry bias during all seasons (Fig. 6). Despite the positive bias, WRF12-remap better captures the seasonal spatial patterns of Q_{PBL} in MERRA-2, leading to positive BSS in all calendar months. Thus, there is added value by higher-resolution simulations in representation of one of the key parameters dictating particle growth and optical properties. Spatial patterns of differences in Q_{PBL} from WRF60 and WRF12-remap relative to MERRA-2 (Fig. 6) exhibit similarities to differences in AOD (Fig. 4). WRF60 is dry-biased relative to WRF12 particularly during the summer (and fall) and underestimates Q_{PBL} relative to MERRA-2 during all seasons over the southern states and over most of continental US during summer and fall. Conversely, WRF12-remap overestimates Q_{PBL} over most of continental US during summer and fall relative to MERRA-2.

$PBLH$ is a key variable for dictating near-surface aerosol concentrations but is highly sensitive to the physical schemes applied, and biases appear to be domain and resolution dependent. However, this parameter is comparatively difficult to assess because differences in $PBLH$ from WRF-Chem and MERRA-2 may also originate from the way they are computed (i.e. from heat diffusivity in MERRA-2 (Jordan et al., 2010) and from turbulent kinetic energy in WRF-Chem (Janjić, 2002;von Engeln and Teixeira, 2013)). Nevertheless, the Mellor-Yamada-Janjich PBL scheme combined with the Noah Land Surface Model applied in this work was found to produce lower PBL heights (Zhang et al., 2009) than other parameterizations. Thus, the positive bias in simulated AOD and surface PM$_{2.5}$ concentrations (reported previously in (Crippa et al., 2016)) may be linked to the systematic underestimation of $PBLH$ simulated by WRF12-remap over continental US relative to MERRA-2 during all seasons (except winter) with greatest bias over regions of complex topography (Fig. S2). A positive bias (of several hundred meters) in terms of $PBLH$ for WRF simulations using the MYJ parameterization was previously reported for high-resolution simulations over complex terrain (Rissman et al., 2013), and a positive bias in $PBLH$ is also observed in the 60 km simulations presented herein (Fig. S2). This may provide a partial explanation for the strong negative bias in AOD in WRF60 during summer (Fig. 3).

443   In general, the BSS indicate improvement in the simulation of *PBLH* in WRF12-remap than in
444   WRF60 (Fig. 7a).

445   Consistent with the dry bias in Q_{PBL} in WRF60, total accumulated precipitation is also
446   underestimated in WRF60, while WRF12-remap captures the absolute magnitudes and the
447   spatial patterns therein (Fig. S3). Analysis of hourly precipitation rates also showed higher skill
448   of WRF12-remap than WRF60 in correctly simulating precipitation occurrence (*HR*) relative
449   to MERRA-2 (Table S2). More specifically WRF12-remap correctly predicts between 40%
450   and 70 % of precipitation events in MERRA-2 with highest skill during winter months, whereas
451   WRF60 output exhibits lower HR (~6% during summer and 30% during winter). This result
452   thus confirms our expectation of a strong sensitivity of model performance to resolution due to
453   the inherent scale dependence in the cumulus scheme.

454   Gas phase concentrations (transformed into z-scores) from WRF12-remap show higher
455   agreement with satellite observations during almost all months, as indicated by the positive
456   BSS (Fig. 7b). However given the limited availability of valid satellite observations (especially
457   during months with low radiation intensity), the BSS are likely only robust for the summer
458   months for all species. Nevertheless, with the exception of NH_3 during June, BSS for all months
459   are above or close to zero indicating that on average, the enhanced resolution simulations do
460   improve the quality of the simulation of the gas phase species even when remapped to 60 km
461   resolution. Further, the seasonal average spatial patterns of the total columnar concentrations,
462   expressed in terms of z-scores, also exhibit qualitative agreement with the satellite observations
463   (Fig. S4-S7).

464   **4 Concluding remarks**

465   This analysis is one of the first to quantify the impact of model spatial resolution on the spatio-
466   temporal variability and magnitude of AOD, and does so using simulations for a full calendar
467   year. Application of WRF-Chem at two different resolutions (60 km and 12 km) over eastern
468   North America for a representative year (2008) leads to the following conclusions:

469   -   Higher resolution simulations add value (i.e. enhance the fidelity of AOD at and near
470   to the peak in the solar spectrum) relative to a coarser run, although the improvement
471   in model performance is not uniform in space and time. Brier Skill Scores for the
472   remapped simulations (i.e. output from simulations conducted at 12 km (WRF12) then
473   averaged to 60 km, WRF12-remap) are positive for ten of twelve calendar moths, and
474   for AOD(λ=550 nm) exceed 0.5 for seven of twelve months.

475   - Spatial correlations of output from WRF12 and WRF12-remap with observations from
476   MODIS are higher than output from a simulation conducted at 60 km during most
477   months. For example, in contrast to WRF-Chem simulations at 60 km (WRF60),
478   simulations conducted at 12 km (WRF12) show positive spatial correlations with
479   MODIS for all λ in all calendar months, and particularly during summer (ρ = 0.5-0.7).

480   - Output from WRF12 and WRF12-remap exhibit highest accord with MODIS
481   observations in capturing the frequency, magnitude and location of extreme AOD
482   values during summer when AOD is typically highest. During May-August WRF12-
483   remap has *Hit Rates* for identification of extreme AOD of 53-78%.

484   - At least some of the improvement in the accuracy with which AOD is reproduced in
485   the higher resolution simulations may be due to improved fidelity of specific humidity
486   and thus more accurate representation of hygroscopic growth of some aerosol
487   components.

488   - Higher-resolution simulations also add value in the representation of other key
489   meteorological variables such as temperature, boundary layer height and precipitation.
490   Both spatial patterns and precipitation occurrence are better captured by WRF12-
491   remap.

492   - More accurate representation of spatial patterns and magnitude of gaseous species that
493   play a key role in particle formation and growth is also achieved by running WRF-
494   Chem at high resolution.

495 It is worthy of note that even the 12 km resolution WRF-Chem simulations exhibit substantial
496 differences in AOD relative to MODIS over eastern North America, and the agreement varies
497 only slightly with wavelength. This may be partially attributable to use of the modal approach
498 to represent the aerosol size distribution in order to enhance computational tractability. In this
499 application each mode has a fixed geometric standard deviation (σ_g), which can lead to biases
500 in simulated AOD in the visible wavelengths by up to 25% (Brock et al., 2016) (with the model
501 overestimating observations if the prescribed σ_g is larger than the observed one). Setting σ_g =
502 2 for the accumulation mode (the default in WRF-Chem) may lead to an overestimation of the
503 number of particles at the end of the accumulation mode tail, and there is evidence that a value
504 of $\sigma_{g,acc}$=1.40 leads to higher agreement with observations (Mann et al., 2012). Further possible
505 sources of the AOD biases reported herein derive from selection of the physical schemes (e.g.
506 planetary boundary layer (*PBL*) schemes and land-surface model (Misenis and Zhang,
507 2010;Zhang et al., 2009)). Further, it is worth mentioning that NEI emissions are specified

based on an average summertime weekday, so enhanced model performance might be achieved if seasonally varying emissions were available. Future work will include a systematic sensitivity analysis of these effects.

Acknowledgments

This research was supported in part by a L'Oréal-UNESCO UK and Ireland Fellowship For Women In Science (to PC), the Natural Environmental Research Council (NERC) through the LICS project (ref. NE/K010794/1), grants to SCP from US NSF (grant # 1517365) and NASA (NNX16AG31G), and a NASA Earth and Space Science Fellowship Program - Grant "14-EARTH14F-0207" (to RCS). Further support was provided by the Lilly Endowment, Inc., through its support for the Indiana University Pervasive Technology Institute and the Indiana METACyt Initiative. We gratefully acknowledge the NASA scientists responsible for MERRA-2 and MODIS products, the developers of WRF-Chem, and Lieven Clarisse, Simon Whitburn, and Martin Van Damme for producing and sharing the NH_3 retrievals.

References

Ackermann, I. J., Hass, H., Memmesheimer, M., Ebel, A., Binkowski, F. S., and Shankar, U.: Modal aerosol dynamics model for Europe: development and first applications, Atmos. Environ., 32, 2981-2999, http://dx.doi.org/10.1016/S1352-2310(98)00006-5, 1998.

Anderson, T. L., Charlson, R. J., Winker, D. M., Ogren, J. A., and Holmén, K.: Mesoscale Variations of Tropospheric Aerosols, Journal of the Atmospheric Sciences, 60, 119-136, doi: http://dx.doi.org/10.1175/1520-0469(2003)060<0119:MVOTA>2.0.CO;2, 2003.

Ångström, A.: The parameters of atmospheric turbidity, Tellus, 16, 64-75, 10.1111/j.2153-3490.1964.tb00144.x, 1964.

Benjamini, Y., and Hochberg, Y.: Controlling the False Discovery Rate: A Practical and Powerful Approach to Multiple Testing, Journal of the Royal Statistical Society. Series B (Methodological), 57, 289-300, 1995.

Boucher, O., D. Randall, P. Artaxo, C. Bretherton, G. Feingold, P. Forster, V.-M. Kerminen, Y. Kondo, H. Liao, U. Lohmann, P. Rasch, S.K. Satheesh, S. Sherwood, B. Stevens and X.Y. Zhang: Clouds and Aerosols, in: Climate Change 2013: The Physical Science Basis. Contribution of Working Group I to the Fifth Assessment Report of the Intergovernmental Panel on Climate Change, edited by: Stocker, T. F., D. Qin, G.-K. Plattner, M. Tignor, S.K. Allen, J. Boschung, A. Nauels, Y. Xia, V. Bex and P.M. Midgley, Cambridge University Press, Cambridge, United Kingdom and New York, NY, USA, 33–115, 2013.

Brinksma, E. J., K. F. Boersma, P. F. Levelt, and R. D. McPeters OMI validation requirements document, Version 1, Rep. RS-OMIE-KNMI-345, 66, 2003.

542 Brock, C. A., Wagner, N. L., Anderson, B. E., Attwood, A. R., Beyersdorf, A., Campuzano-
543 Jost, P., Carlton, A. G., Day, D. A., Diskin, G. S., Gordon, T. D., Jimenez, J. L., Lack, D. A.,
544 Liao, J., Markovic, M. Z., Middlebrook, A. M., Ng, N. L., Perring, A. E., Richardson, M. S.,
545 Schwarz, J. P., Washenfelder, R. A., Welti, A., Xu, L., Ziemba, L. D., and Murphy, D. M.:
546 Aerosol optical properties in the southeastern United States in summer – Part 1: Hygroscopic
547 growth, Atmos. Chem. Phys., 16, 25695-25738, doi:10.5194/acp-16-5009-2016, 2016.

548 Chance, K.: OMI algorithm theoretical basis document, volume IV: OMI trace gas
549 algorithms, 2002.

550 Chen, F., and Dudhia, J.: Coupling an advanced land surface–hydrology model with the Penn
551 State–NCAR MM5 modeling system. Part I: model implementation and sensitivity, Monthly
552 Weather Review, 129, 569-585, doi:10.1175/1520-
553 0493(2001)129<0569:CAALSH>2.0.CO;2, 2001.

554 Chin, M., Kahn, R. A., and Schwartz , S. E.: Atmospheric Aerosols Properties and Climate
555 Impacts. A Report by the U.S. Climate Change Science Program and the Subcommittee on
556 Global Change Research, in, National Aeronautics and Space Administration, Washington,
557 D.C., USA, 128, 2009.

558 Crippa, P., Sullivan, R. C., Thota, A., and Pryor, S. C.: Evaluating the skill of high-resolution
559 WRF-Chem simulations in describing drivers of aerosol direct climate forcing on the regional
560 scale, Atmos. Chem. Phys., 16, 397-416, 10.5194/acp-16-397-2016, 2016.

561 Di Luca, A., de Elía, R., and Laprise, R.: Challenges in the Quest for Added Value of
562 Regional Climate Dynamical Downscaling, Curr Clim Change Rep, 1, 10-21,
563 10.1007/s40641-015-0003-9, 2015.

564 Diaconescu, E., and Laprise, R.: Can added value be expected in RCM-simulated large
565 scales?, Clim Dyn, 41, 1769-1800, 10.1007/s00382-012-1649-9, 2013.

566 Emmons, L. K., Walters, S., Hess, P. G., Lamarque, J. F., Pfister, G. G., Fillmore, D.,
567 Granier, C., Guenther, A., Kinnison, D., Laepple, T., Orlando, J., Tie, X., Tyndall, G.,
568 Wiedinmyer, C., Baughcum, S. L., and Kloster, S.: Description and evaluation of the Model
569 for Ozone and Related chemical Tracers, version 4 (MOZART-4), Geoscientific Model
570 Development, 3, 43-67, doi:10.5194/gmd-3-43-2010, 2010.

571 Fast, J. D., Gustafson, W. I., Easter, R. C., Zaveri, R. A., Barnard, J. C., Chapman, E. G.,
572 Grell, G. A., and Peckham, S. E.: Evolution of ozone, particulates, and aerosol direct
573 radiative forcing in the vicinity of Houston using a fully coupled meteorology-chemistry-
574 aerosol model, Journal of Geophysical Research: Atmospheres, 111, D21305,
575 10.1029/2005JD006721, 2006.

576 Fioletov, V. E., McLinden, C. A., Krotkov, N., Moran, M. D., and Yang, K.: Estimation of
577 SO_2 emissions using OMI retrievals, Geophysical Research Letters, 38, L21811,
578 10.1029/2011GL049402, 2011.

579 Flores, J. M., Bar-Or, R. Z., Bluvshtein, N., Abo-Riziq, A., Kostinski, A., Borrmann, S.,
580 Koren, I., Koren, I., and Rudich, Y.: Absorbing aerosols at high relative humidity: linking
581 hygroscopic growth to optical properties, Atmospheric Chemistry and Physics, 12, 5511-
582 5521, 10.5194/acp-12-5511-2012, 2012.

583   Grell, G. A., and Dévényi, D.: A generalized approach to parameterizing convection
584   combining ensemble and data assimilation techniques, Geophysical Research Letters, 29, 38-
585   31-38-34, 10.1029/2002GL015311, 2002.

586   Grell, G. A., Peckham, S. E., Schmitz, R., McKeen, S. A., Frost, G., Skamarock, W. C., and
587   Eder, B.: Fully coupled "online" chemistry within the WRF model, Atmos. Environ., 39,
588   6957-6975, 10.1016/j.atmosenv.2005.04.027, 2005.

589   Guenther, A., Zimmerman, P., and Wildermuth, M.: Natural volatile organic compound
590   emission rate estimates for U.S. woodland landscapes, Atmos. Environ., 28, 1197-1210,
591   10.1016/1352-2310(94)90297-6, 1994.

592   Guenther, A. B., Zimmerman, P. R., Harley, P. C., Monson, R. K., and Fall, R.: Isoprene and
593   monoterpene emission rate variability: model evaluations and sensitivity analyses, J.
594   Geophys. Res.-Atmos., 98, 12609-12617, 10.1029/93jd00527, 1993.

595   Gustafson, W. I., Qian, Y., and Fast, J. D.: Downscaling aerosols and the impact of neglected
596   subgrid processes on direct aerosol radiative forcing for a representative global climate model
597   grid spacing, Journal of Geophysical Research: Atmospheres, 116, D13303,
598   10.1029/2010JD015480, 2011.

599   Hong, S.-Y., Dudhia, J., and Chen, S.-H.: A Revised Approach to Ice Microphysical
600   Processes for the Bulk Parameterization of Clouds and Precipitation, Monthly Weather
601   Review, 132, 103-120, doi:10.1175/1520-0493(2004)132<0103:ARATIM>2.0.CO;2, 2004.

602   Hyer, E. J., Reid, J. S., and Zhang, J.: An over-land aerosol optical depth data set for data
603   assimilation by filtering, correction, and aggregation of MODIS Collection 5 optical depth
604   retrievals, Atmospheric Measurement Techniques, 4, 379-408, 10.5194/amt-4-379-2011,
605   2011.

606   Janjić, Z. I.: The Step-Mountain Eta Coordinate Model: Further Developments of the
607   Convection, Viscous Sublayer, and Turbulence Closure Schemes, Monthly Weather Review,
608   122, 927-945, doi:10.1175/1520-0493(1994)122<0927:TSMECM>2.0.CO;2, 1994.

609   Janjić, Z. I.: Nonsingular implementation of the Mellor–Yamada level 2.5 scheme in the
610   NCEP Meso model, NCEP office note, 437, 61, 2002.

611   Jordan, N. S., Hoff, R. M., and Bacmeister, J. T.: Validation of Goddard Earth Observing
612   System-version 5 MERRA planetary boundary layer heights using CALIPSO, J. Geophys.
613   Res.-Atmos., 115, 10.1029/2009jd013777, 2010.

614   Krotkov, N. A., McClure, B., Dickerson, R. R., Carn, S. A., Li, C., Bhartia, P. K., Yang, K.,
615   Krueger, A. J., Li, Z., Levelt, P. F., Chen, H., Wang, P., and Lu, D.: Validation of SO_2
616   retrievals from the Ozone Monitoring Instrument over NE China, Journal of Geophysical
617   Research: Atmospheres, 113, D16S40, 10.1029/2007JD008818, 2008.

618   Leibensperger, E., Mickley, L. J., Jacob, D. J., Chen, W.-T., Seinfeld, J., Nenes, A., Adams,
619   P., Streets, D., Kumar, N., and Rind, D.: Climatic effects of 1950–2050 changes in US
620   anthropogenic aerosols–Part 1: Aerosol trends and radiative forcing, Atmospheric Chemistry
621   and Physics, 12, 3333-3348, doi:10.5194/acp-12-3333-2012, 2012.

Levy, R. C., Mattoo, S., Munchak, L. A., Remer, L. A., Sayer, A. M., Patadia, F., and Hsu, N. C.: The Collection 6 MODIS aerosol products over land and ocean, Atmospheric Measurement Techniques, 6, 2989-3034, 10.5194/amt-6-2989-2013, 2013.

Long, M., Yantosca, R., Nielsen, J., Keller, C., da Silva, A., Sulprizio, M., Pawson, S., and Jacob, D.: Development of a grid-independent GEOS-Chem chemical transport model (v9-02) as an atmospheric chemistry module for Earth system models, Geoscientific Model Development, 8, 595-602, doi:10.5194/gmd-8-595-2015, 2015.

Mann, G. W., Carslaw, K. S., Ridley, D. A., Spracklen, D. V., Pringle, K. J., Merikanto, J., Korhonen, H., Schwarz, J. P., Lee, L. A., Manktelow, P. T., Woodhouse, M. T., Schmidt, A., Breider, T. J., Emmerson, K. M., Reddington, C. L., Chipperfield, M. P., and Pickering, S. J.: Intercomparison of modal and sectional aerosol microphysics representations within the same 3-D global chemical transport model, Atmospheric Chemistry and Physics, 12, 4449-4476, 10.5194/acp-12-4449-2012, 2012.

Martin, S. T., Hung, H. M., Park, R. J., Jacob, D. J., Spurr, R. J. D., Chance, K. V., and Chin, M.: Effects of the physical state of tropospheric ammonium-sulfate-nitrate particles on global aerosol direct radiative forcing, Atmospheric Chemistry and Physics, 4, 183-214, doi:10.5194/acp-4-183-2004, 2004.

McComiskey, A., Schwartz, S. E., Schmid, B., Guan, H., Lewis, E. R., Ricchiazzi, P., and Ogren, J. A.: Direct aerosol forcing: Calculation from observables and sensitivities to inputs, Journal of Geophysical Research: Atmospheres, 113, D09202, 10.1029/2007JD009170, 2008.

McLinden, C. A., Fioletov, V., Boersma, K. F., Kharol, S. K., Krotkov, N., Lamsal, L., Makar, P. A., Martin, R. V., Veefkind, J. P., and Yang, K.: Improved satellite retrievals of NO_2 and SO_2 over the Canadian oil sands and comparisons with surface measurements, Atmos. Chem. Phys., 14, 3637-3656, 10.5194/acp-14-3637-2014, 2014.

Meehl, G. A., Moss, R., Taylor, K. A., Eyring, V., Stouffer, R. J., Sandrine, B., and Stevens, B.: Climate model intercomparisons: preparing for the next phase, Eos, Transaction, American Geophysical Union, 95, 77-84, doi:10.1002/2014EO09, 2014.

Misenis, C., and Zhang, Y.: An examination of sensitivity of WRF/Chem predictions to physical parameterizations, horizontal grid spacing, and nesting options, Atmospheric Research, 97, 315-334, 10.1016/j.atmosres.2010.04.005, 2010.

Mlawer, E. J., Taubman, S. J., Brown, P. D., Iacono, M. J., and Clough, S. A.: Radiative transfer for inhomogeneous atmospheres: RRTM, a validated correlated-k model for the longwave, Journal of Geophysical Research: Atmospheres, 102, 16663-16682, 10.1029/97JD00237, 1997.

Molod, A., Takacs, L., Suarez, M., and Bacmeister, J.: Development of the GEOS-5 atmospheric general circulation model: evolution from MERRA to MERRA2, Geoscientific Model Development, 8, 1339-1356, 10.5194/gmd-8-1339-2015, 2015.

Murphy, A. H., and Epstein, E. S.: Skill scores and correlation-coefficients in model verification, Monthly Weather Review, 117, 572-581, 10.1175/1520-0493(1989)117<0572:ssacci>2.0.co;2, 1989.

662 Myhre, G., Samset, B. H., Schulz, M., Balkanski, Y., Bauer, S., Berntsen, T. K., Bian, H.,
663 Bellouin, N., Chin, M., Diehl, T., Easter, R. C., Feichter, J., Ghan, S. J., Hauglustaine, D.,
664 Iversen, T., Kinne, S., Kirkevag, A., Lamarque, J. F., Lin, G., Liu, X., Lund, M. T., Luo, G.,
665 Ma, X., van Noije, T., Penner, J. E., Rasch, P. J., Ruiz, A., Seland, O., Skeie, R. B., Stier, P.,
666 Takemura, T., Tsigaridis, K., Wang, P., Wang, Z., Xu, L., Yu, H., Yu, F., Yoon, J. H., Zhang,
667 K., Zhang, H., and Zhou, C.: Radiative forcing of the direct aerosol effect from AeroCom
668 Phase II simulations, Atmospheric Chemistry and Physics, 13, 1853-1877, 10.5194/acp-13-
669 1853-2013, 2013a.

670 Myhre, G., Shindell, D., Bréon, F.-M., Collins, W., Fuglestvedt, J., Huang, J., Koch, D.,
671 Lamarque, J.-F., Lee, D., Mendoza, B., Nakajima, T., Robock, A., Stephens, G., Takemura,
672 T., and Zhang, H.: Anthropogenic and Natural Radiative Forcing, in: Climate Change 2013:
673 The Physical Science Basis. Contribution of Working Group I to the Fifth Assessment Report
674 of the Intergovernmental Panel on Climate Change, edited by: Stocker, T. F., Qin, D.,
675 Plattner, G.-K., Tignor, M., Allen, S. K., Boschung, J., Nauels, A., Xia, Y., Bex, V., and
676 Midgley, P. M., Cambridge University Press, Cambridge, United Kingdom and New York,
677 NY, USA, 659–740, 2013b.

678 Qian, Y., Gustafson Jr, W. I., and Fast, J. D.: An investigation of the sub-grid variability of
679 trace gases and aerosols for global climate modeling, Atmos. Chem. Phys., 10, 6917-6946,
680 10.5194/acp-10-6917-2010, 2010.

681 Rissman, J., Arunachalam, S., Woody, M., West, J. J., BenDor, T., and Binkowski, F. S.: A
682 plume-in-grid approach to characterize air quality impacts of aircraft emissions at the
683 Hartsfield–Jackson Atlanta International Airport, Atmos. Chem. Phys., 13, 9285-9302,
684 10.5194/acp-13-9285-2013, 2013.

685 Rockel, B., Castro, C. L., Pielke, R. A., von Storch, H., and Leoncini, G.: Dynamical
686 downscaling: Assessment of model system dependent retained and added variability for two
687 different regional climate models, Journal of Geophysical Research: Atmospheres, 113,
688 D21107, 10.1029/2007JD009461, 2008.

689 Santarpia, J. L., Gasparini, R., Li, R. J., and Collins, D. R.: Diurnal variations in the
690 hygroscopic growth cycles of ambient aerosol populations, J. Geophys. Res.-Atmos., 110,
691 10.1029/2004jd005279, 2005.

692 Schell, B., Ackermann, I. J., Hass, H., Binkowski, F. S., and Ebel, A.: Modeling the
693 formation of secondary organic aerosol within a comprehensive air quality model system, J.
694 Geophys. Res.-Atmos., 106, 28275-28293, 10.1029/2001jd000384, 2001.

695 Schuster, G. L., O. Dubovik, and B. N. Holben Angstrom exponent and bimodal aerosol size
696 distributions, J. Geophys. Res.-Atmos., 111, D07207, doi:10.1029/2005JD006328., 2006.

697 Seinfeld, J. H., and Pandis, S. N.: Atmospheric chemistry and physics: from air pollution to
698 climate change, John Wiley & Sons, 1152 pp., 2016.

699 Simes, R. J.: An improved Bonferroni procedure for multiple tests of significance,
700 Biometrika, 73, 751-754, 10.2307/2336545, 1986.

Simpson, D., Guenther, A., Hewitt, C. N., and Steinbrecher, R.: Biogenic emissions in Europe. 1. estimates and uncertainties, J. Geophys. Res.-Atmos., 100, 22875-22890, 10.1029/95jd02368, 1995.

Stocker, T. F. a. Q., D. and Plattner, G.-K. and Alexander, L.V. and Allen, S.K. and Bindoff, N.L. and Bréon, F.-M. and Church, J.A. and Cubasch, U. and Emori, S. and Forster, P. and Friedlingstein, P. and Gillett, N. and Gregory, J.M. and Hartmann, D.L. and Jansen, E. and Kirtman, B. and Knutti, R. and Krishna Kumar, K. and Lemke, P. and Marotzke, J. and Masson-Delmotte, V. and Meehl, G.A. and Mokhov, I.I. and Piao, S. and Ramaswamy, V. and Randall, D. and Rhein, M. and Rojas, M. and Sabine, C. and Shindell, D. and Talley, L.D. and Vaughan, D.G. and Xie, S.-P.: Summary for Policymakers, in: Climate Change 2013: The Physical Science Basis. Contribution of Working Group I to the Fifth Assessment Report of the Intergovernmental Panel on Climate Change, Cambridge University Press, Cambridge, United Kingdom and New York, NY, USA, 33–115, 2013.

Stockwell, W. R., Middleton, P., Chang, J. S., and Tang, X.: The second generation regional acid deposition model chemical mechanism for regional air quality modeling, Journal of Geophysical Research: Atmospheres, 95, 16343-16367, 10.1029/JD095iD10p16343, 1990.

Taylor, K. E.: Summarizing multiple aspects of model performance in a single diagram, J. Geophys. Res.-Atmos., 106, 7183-7192, 10.1029/2000jd900719, 2001.

Tilmes, S., Lamarque, J.-F., Emmons, L., Kinnison, D., Ma, P.-L., Liu, X., Ghan, S., Bardeen, C., Arnold, S., and Deeter, M.: Description and evaluation of tropospheric chemistry and aerosols in the Community Earth System Model (CESM1. 2), Geoscientific Model Development, 8, 1395-1426, doi:10.5194/gmd-8-1395-2015, 2015.

Tomasi, C., Caroli, E., and Vitale, V.: Study of the Relationship between Ångström's Wavelength Exponent and Junge Particle Size Distribution Exponent, Journal of Climate and Applied Meteorology, 22, 1707-1716, 10.1175/1520-0450(1983)022<1707:SOTRBW>2.0.CO;2, 1983.

US-EPA: 2005 National Emissions Inventory (NEI), US Environmental Protection Agency in, available at: ftp://aftp.fsl.noaa.gov/divisions/taq/emissions_data_2005/, 2009.

Vinken, G. C. M., Boersma, K. F., van Donkelaar, A., and Zhang, L.: Constraints on ship NO_x emissions in Europe using GEOS-Chem and OMI satellite NO_2 observations, Atmos. Chem. Phys., 14, 1353-1369, 10.5194/acp-14-1353-2014, 2014.

von Engeln, A., and Teixeira, J.: A Planetary Boundary Layer Height Climatology Derived from ECMWF Reanalysis Data, Journal of Climate, 26, 6575–6590, doi: 10.1175/JCLI-D-12-00385.1, 2013.

Weigum, N., Schutgens, N., and Stier, P.: Effect of aerosol sub-grid variability on aerosol optical depth and cloud condensation nuclei: Implications for global aerosol modelling, Atmos. Chem. Phys. Discuss., 2016, 1-36, 10.5194/acp-2016-360, 2016.

Whitburn, S., Van Damme, M., Clarisse, L., Bauduin, S., Heald, C., Hadji-Lazaro, J., Hurtmans, D., Zondlo, M. A., Clerbaux, C., Coheur, P.-F.: A flexible and robust neural network IASI-NH_3 retrieval algorithm, J. Geophys. Res. Atmos, In Press, 10.1002/2016JD024828, 2016.

742   Wild, O., Zhu, X., and Prather, M. J.: Fast-J: Accurate Simulation of In- and Below-Cloud
743   Photolysis in Tropospheric Chemical Models, Journal of Atmospheric Chemistry, 37, 245-
744   282, 10.1023/a:1006415919030, 2000.

745   Zhang, Y., Dubey, M. K., Olsen, S. C., Zheng, J., and Zhang, R.: Comparisons of
746   WRF/Chem simulations in Mexico City with ground-based RAMA measurements during the
747   2006-MILAGRO, Atmospheric Chemistry and Physics, 9, 3777-3798, doi:10.5194/acp-9-
748   3777-2009, 2009.

749   Zieger, P., Fierz-Schmidhauser, R., Weingartner, E., and Baltensperger, U.: Effects of
750   relative humidity on aerosol light scattering: results from different European sites,
751   Atmospheric Chemistry and Physics, 13, 10609-10631, 10.5194/acp-13-10609-2013, 2013.

752

753
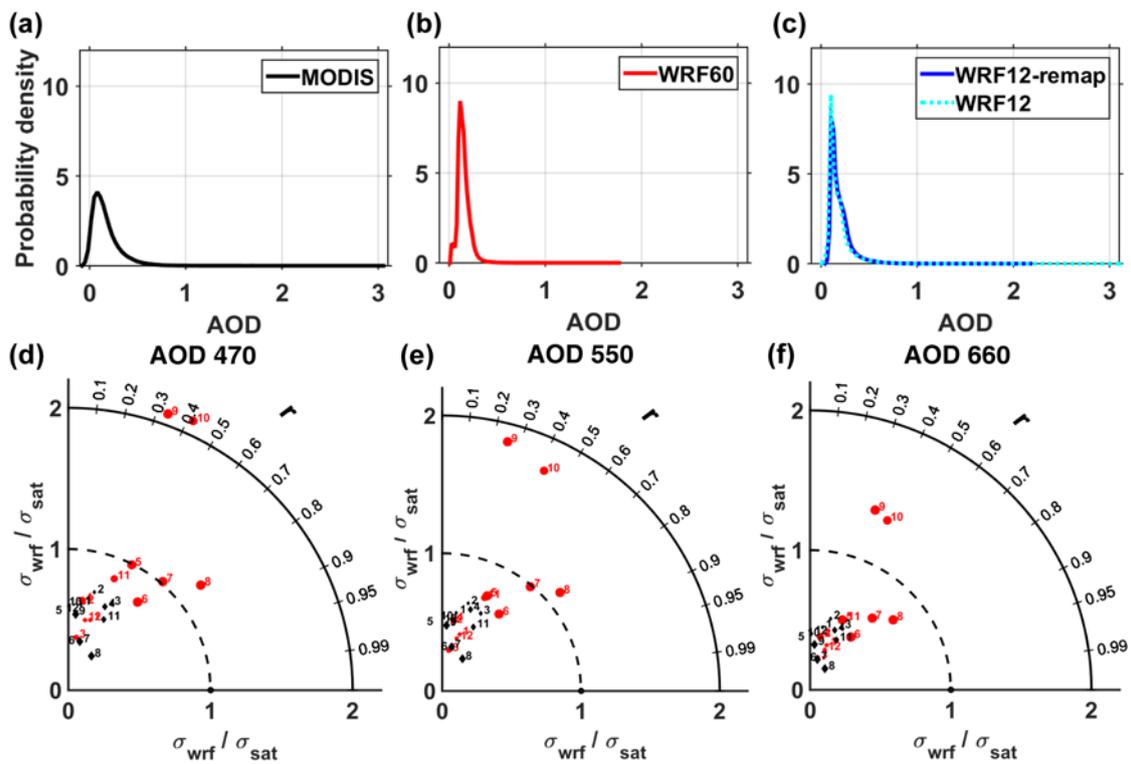
Figures

Figure 1. Probability density function of once daily AOD at a wavelength (λ) of 550 nm for (a) MODIS, (b) WRF60 and (c) WRF12 and WRF12-remap during the year 2008. (d-f) Taylor diagrams of mean monthly AOD at wavelengths (λ) of (d) 470, (e) 550 and (f) 660 nm as simulated by WRF-Chem at different resolutions (black diamonds=WRF60 and red dots=WRF12-remap) relative to MODIS observations. The numbers by each symbol denote the calendar month (e.g. 1=January).
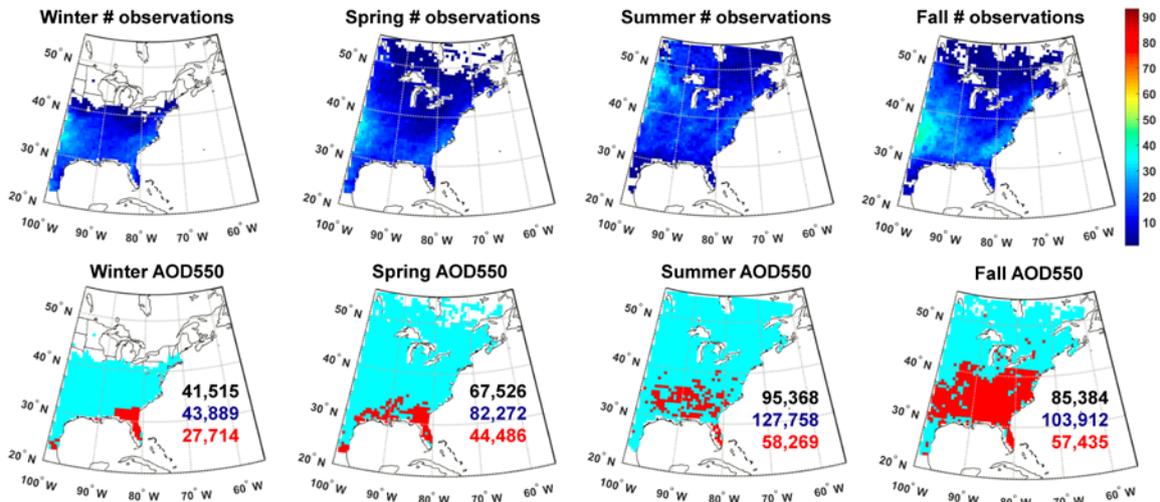
Figure 2. First line: Number of paired AOD observations at a wavelength (λ) of 550 nm (i.e. simultaneous values as output from WRF-Chem and observed by MODIS) used to perform a t-test designed to evaluate whether the difference computed for each grid cell as WRF60-MODIS differs from that computed as WRF12-remap-MODIS on a seasonal basis (columns show Winter (DJF), Spring (MAM), Summer (JJA) and Fall (SON)). Second line: Results of the t-test. Pixels that have p-values that are significantly different at α=0.10 are indicated in red and have been corrected for multiple testing using a False Discovery Rate approach. The number of observations of cloud-free conditions summed across all days in each season and all grid cells is also reported (black=MODIS, blue=WRF60, red=WRF12-remap).
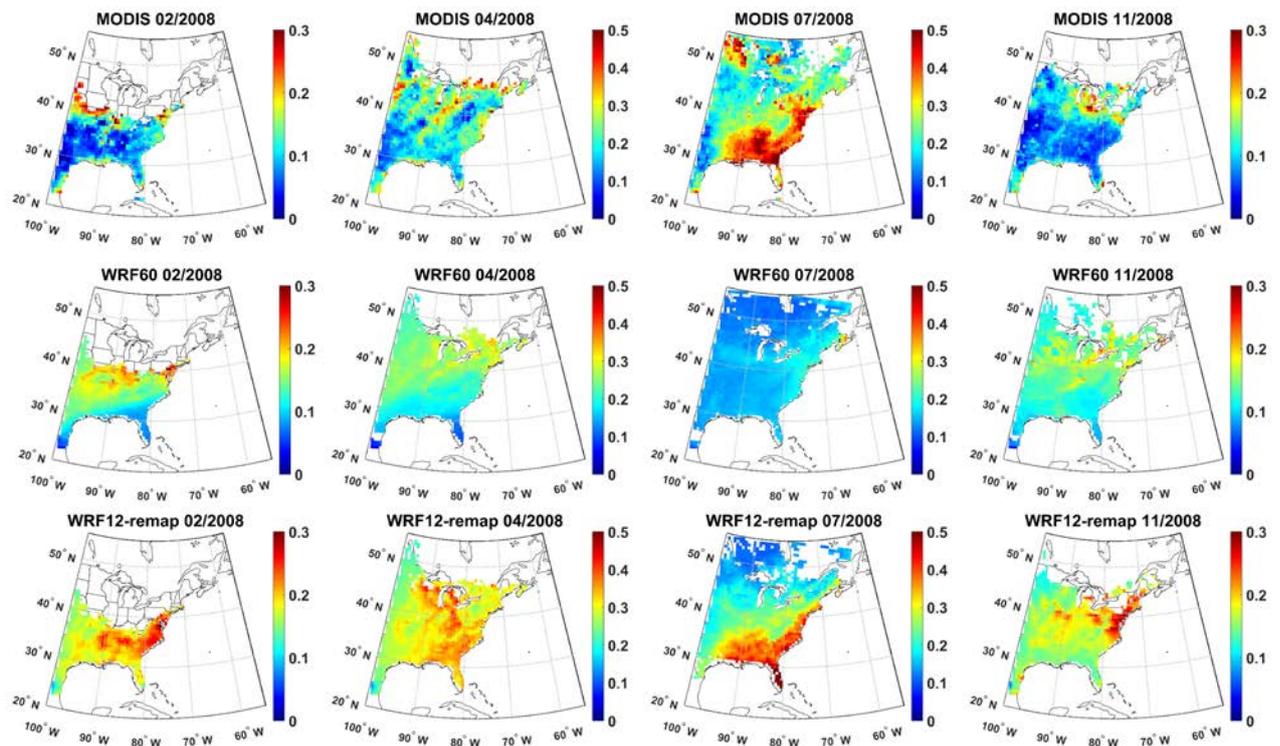
Figure 3. Monthly mean AOD at a wavelength (λ) of 550 nm from MODIS (first line) and WRF-Chem at different resolutions (WRF60 and WRF12-remap, second and third line) during a representative month in each climatological season (columns). Note that a different color scale is applied for different months. For a monthly mean value for a grid cell to be shown, there must be at least 5-simultaneous daily values (for the time of the satellite overpass) available.

784
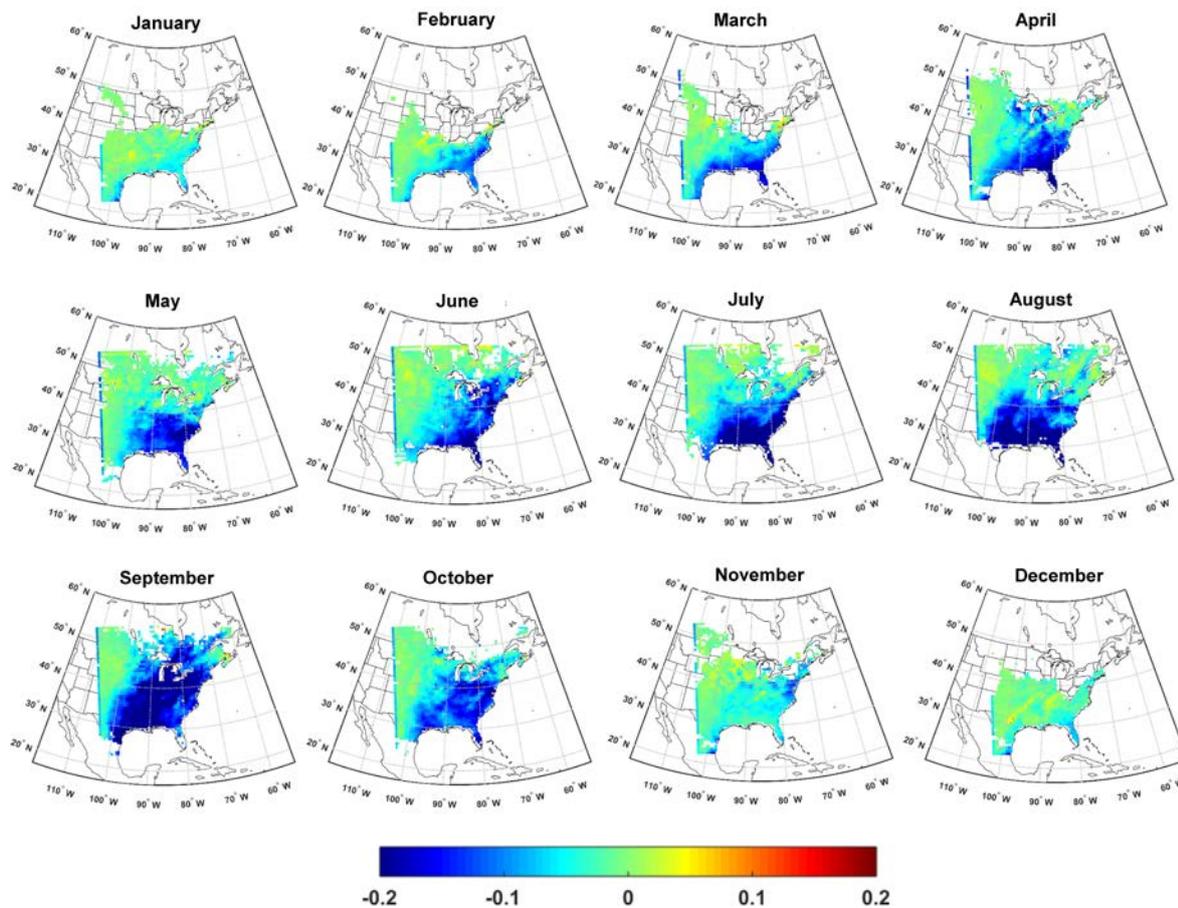
Figure 4. Difference in monthly mean AOD at a wavelength (λ) of 550 nm between WRF-Chem simulations conducted at 60 km resolution (WRF60) and output from WRF-Chem simulations conducted with a resolution of 12 km but remapped to 60 km (WRF12-remap). Differences are computed as WRF60 minus WRF12-remap. Similar spatial patterns and magnitudes of differences are found for λ of 470 and 660 nm. The calendar months of 2008 are shown in the titles of each panel.

792
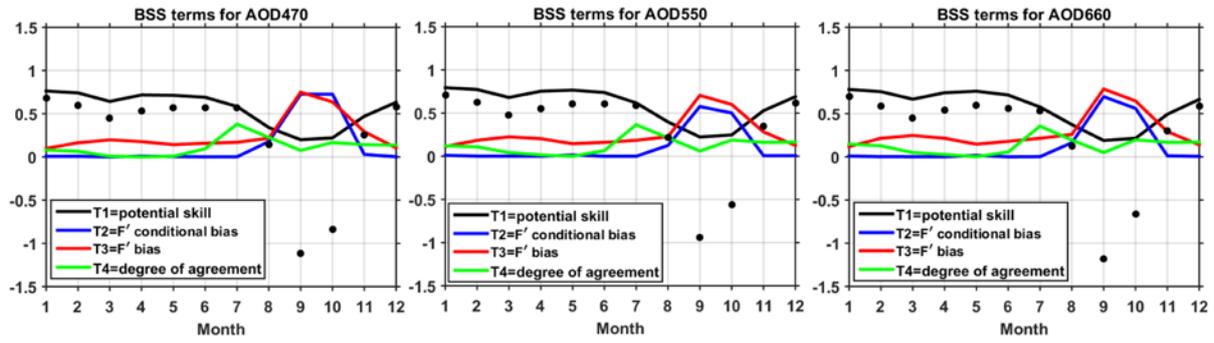
Figure 5. Brier Skill Scores (BSS, black dots) for monthly mean AOD by calendar month (1=January) for AOD at 470, 550 and 660 nm. In this analysis of model skill WRF12 output is mapped to the WRF60 grid (WRF12-remap) and BSS are computed using MODIS as the target, WRF60 as the reference forecast and WRF12-remap as the forecast. Also shown by the color lines are the contributions of different terms to BSS.

798

799
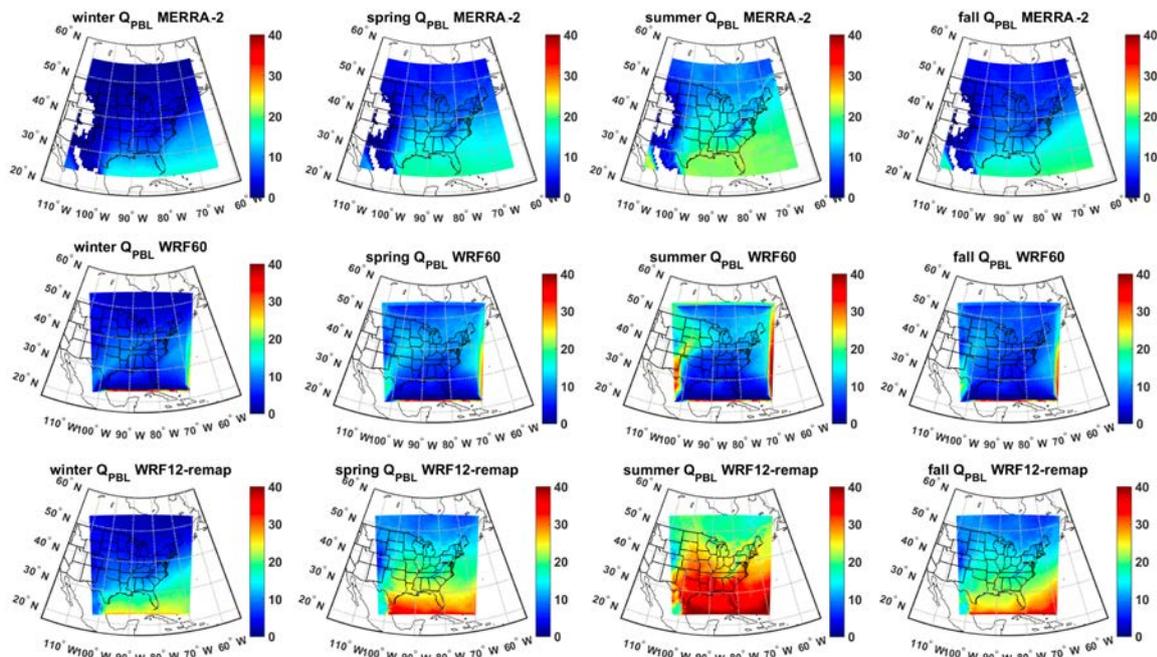
Figure 6. Seasonal mean specific humidity [kg m⁻²] integrated from the surface to 825 hPa

(Q_{PBL}) **from MERRA-2 (first row) assuming an average air density in the** *PBL* **of 1.1 kg**

m⁻³, WRF60 (second row), and WRF12-remap (third row). The data are 3-hourly and

show only cloud-free hours in all three data sets.

804
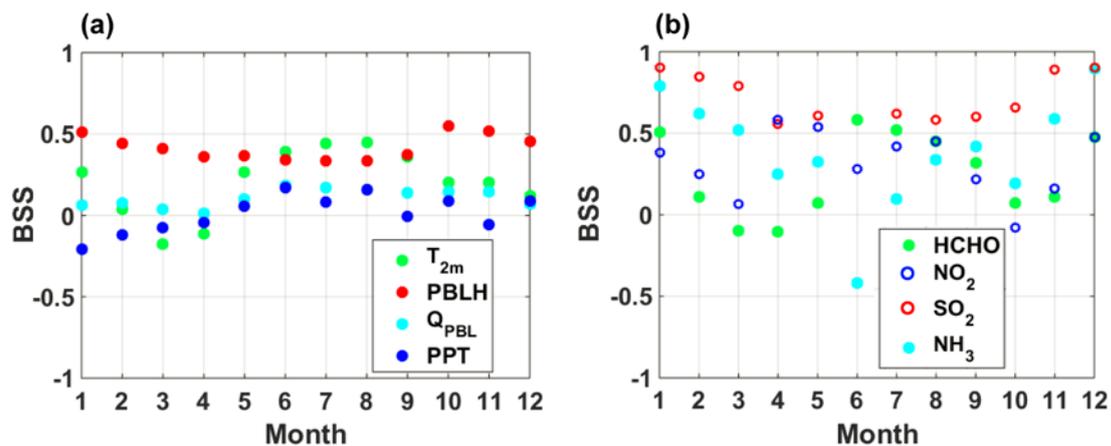
805

806 **Figure 7. Brier Skill Scores (BSS) for key (a) meteorological and (b) chemical variables.**

807 **BSS are computed using hourly data of T at 2m (T_{2m}) and *PBLH*, 3-hourly estimates of**

808 **specific humidity in the boundary layer (Q_{PBL}), and z-scores of monthly total precipitation**

809 **(*PPT*), and of monthly mean columnar gas phase concentrations.**

810

811

812 **Tables**

813 **Table 1. Physical and chemical schemes adopted in the WRF-Chem simulations presented**

814 **herein.**

Simulation settings	Values
Domain size	300 × 300 (60 × 60) grid points
Horizontal resolution	12 km (60 km)
Vertical resolution	32 levels up to 50 hPa
Timestep for physics	72 s (300 s)
Timestep for chemistry	5 s
Physics option	**Adopted scheme**
Microphysics	WRF Single-Moment 5-class (Hong et al., 2004)
Longwave Radiation	Rapid Radiative Transfer Model (RRTM) (Mlawer et al., 1997)
Shortwave Radiation	Goddard (Fast et al., 2006)
Surface layer	Monin Obhukov similarity (Janjić, 2002;Janjić, 1994)
Land Surface	Noah Land Surface Model (Chen and Dudhia, 2001)
Planetary boundary layer	Mellor-Yamada-Janjich (Janjić, 1994)
Cumulus parameterizations	Grell 3 (Grell and Dévényi, 2002)
Chemistry option	**Adopted scheme**
Photolysis	Fast J (Wild et al., 2000)
Gas-phase chemistry	RADM2 (Stockwell et al., 1990)
Aerosols	MADE/SORGAM (Ackermann et al., 1998;Schell et al., 2001)
Anthropogenic emissions	NEI (2005) (US-EPA, 2009)
Biogenic emissions	Guenther, from USGS land use classification (Guenther et al., 1994;Guenther et al., 1993;Simpson et al., 1995)

815

816

Table 2. Spearman correlation coefficients (ρ) between AOD at wavelengths (λ) of 470, 550 and 660 nm from MODIS observations averaged over 12 or 60 km and WRF-Chem simulations conducted at 60 km (WRF60, shown in the table as -60), at 12 km (WRF12, shown in the table as -12), and from WRF-Chem simulations at 12 km but remapped to 60 km (WRF12-remap, shown in the table as -remap). Given WRF12-remap is obtained by averaging WRF12 when at least half of the 5×5 12 km resolution cells contain valid data, ρ from WRF60 and WRF12-remap may be computed on slightly different observations and sample size. The bold text denotes correlation coefficients that are significant at α=0.05 after a Bonferroni correction is applied (i.e. $p \le \frac{0.05}{9 \times 12} = 4.63 \times 10^{-4}$ is significant). The yellow shading is a visual guide that shows for each month and λ the model output that has highest ρ with MODIS.

Month→/Variable↓	Jan	Feb	Mar	Apr	May	Jun	Jul	Aug	Sep	Oct	Nov	Dec
470-12	**0.238**	**0.150**	**0.137**	**0.147**	**0.377**	**0.581**	**0.610**	**0.723**	**0.352**	**0.306**	**0.259**	**0.212**
470-60	0.156	**0.226**	**0.438**	**0.412**	-0.219	-0.146	**0.379**	**0.601**	0.087	-0.051	**0.500**	-0.059
470-remap	**0.295**	**0.197**	**0.250**	**0.182**	**0.516**	**0.637**	**0.675**	**0.777**	**0.368**	**0.441**	**0.315**	**0.274**
550-12	0.223	0.124	0.142	0.146	0.349	0.541	0.580	0.689	0.275	0.301	0.280	0.215
550-60	**0.179**	**0.244**	**0.429**	**0.332**	-0.288	-0.188	0.324	0.567	0.073	-0.077	**0.491**	0.002
550-remap	**0.297**	0.164	0.261	0.199	**0.493**	**0.605**	**0.651**	**0.747**	0.286	0.437	0.352	**0.309**
660-12	0.217	0.136	0.165	0.152	0.324	0.476	0.540	0.644	0.183	0.290	0.292	0.221
660-60	0.191	**0.230**	**0.437**	**0.402**	-0.305	-0.189	0.389	0.616	0.099	-0.137	**0.536**	0.049
660-remap	**0.356**	0.211	0.289	0.208	**0.480**	**0.624**	**0.669**	**0.772**	**0.371**	0.432	0.393	**0.368**

Table 3. Spatial coherence in the identification of extreme AOD values (i.e. areas with AOD>75th percentile over space for each month) between WRF-Chem at different resolutions relative to MODIS. No significant wavelength dependence is found for model skill in identifying extreme AOD so results are only shown for λ = 550 nm. The different model output is denoted by -60 for simulations at 60 km, -12 for simulations at 12 km resolution, and as –remap for simulations at 12 km but with the output remapped to 60 km. The *Accuracy* (Acc) indicates the fraction of grid cells co-identified as extremes and non-extremes between WRF-Chem and MODIS relative to the total number of cells with valid data. The *Hit Rate* (*HR*) is the probability of correct forecast and is the proportion of cells correctly identified as extremes by both WRF-Chem and MODIS. The yellow shading indicates the model resolution with highest skill in each month for AOD at 550 nm.

Month→/ Metric↓	Jan	Feb	Mar	Apr	May	Jun	Jul	Aug	Sep	Oct	Nov	Dec
Acc-12	0.673	0.665	0.659	0.638	0.710	0.800	0.855	0.839	0.666	0.679	0.723	0.661
Acc-60	0.707	0.778	0.735	0.730	0.600	0.587	0.658	0.769	0.661	0.637	0.729	0.681
Acc-remap	0.674	0.680	0.694	0.640	0.766	0.824	0.887	0.837	0.667	0.699	0.767	0.641
HR-12	0.346	0.331	0.319	0.275	0.421	0.599	0.711	0.678	0.333	0.358	0.447	0.323
HR-60	0.417	0.558	0.471	0.460	0.200	0.173	0.315	0.538	0.321	0.274	0.458	0.364
HR-remap	0.350	0.361	0.387	0.281	0.532	0.649	0.775	0.674	0.333	0.399	0.535	0.284